JGR Space Physics

RESEARCH ARTICLE
10.1029/2021JA029955

Asymmetrically Varying Guide Field During Magnetic Reconnection: Particle-In-Cell Simulations

Susanne F. Spinnangr[1], Paul Tenfjord[1], Michael Hesse[2], Cecilia Norgren[1], Håkon M. Kolstø[1], Norah K. Kwagala[1], Therese Moretto Jørgensen[2], and Judit Pérez-Coll Jiménez[1]

[1]Space Plasma Physics Group, University of Bergen, Bergen, Norway, [2]NASA's Ames Research Center, Mountain View, CF, USA

Key Points:

- Spatio-temporal effects in the inflow conditions causes modulations in the reconnection rate and introduces time-dependent effects
- The asymmetrically varying guide field alters the force balance between the current sheet and inflow region
- The outflow regions show nonlaminar exhaust structures induced by the changing inflow

Correspondence to:

S. F. Spinnangr,
susanne.spinnangr@uib.no

Citation:

Spinnangr, S. F., Tenfjord, P., Hesse, M., Norgren, C., Kolstø, H. M., Kwagala, N. K., et al. (2022). Asymmetrically varying guide field during magnetic reconnection: Particle-in-cell simulations. *Journal of Geophysical Research: Space Physics*, *127*, e2021JA029955. https://doi.org/10.1029/2021JA029955

Received 9 SEP 2021
Accepted 6 DEC 2021

Abstract Using fully kinetic particle-in-cell modeling, we investigate how magnetic reconnection responds to a varying guide field in one of the inflow regions. We find that the reconnection rate varies significantly when the orientation of the magnetic field changes between being strictly antiparallel and having a guide field. These variations are fairly consistent with the scaling relation for asymmetric reconnection developed by Cassak and Shay (2007). However, the rate is also found to be nonlinearly modulated by changes in the ion inflow velocity. The spatio-temporal change in the inflow velocity arises as the magnetic forces reconfigure to regions of different magnetic field strengths. The variations in the inflow magnetic field configuration allow for different gradients in the magnetic field, leading to asymmetries in the magnetic tension force. By momentum conservation, this facilitates asymmetries in the inflow velocity, which in turn affects the flux transport into the reconnection site. The outflow is found to be less laminar when the inflow varies, and various signatures of the inflow variations are identified in the outflow.

Plain Language Summary Magnetic reconnection can be described as magnetic explosions, where energy stored in magnetic fields is converted into heat and movement of particles. It can happen in all environments where magnetic fields and charged particles interact, such as in the Sun, in planetary magnetospheres, and in fusion reactors on Earth. In this article, using numerical simulations, we present new insight into how magnetic reconnection behaves when the magnetic fields vary during the reconnection process.

1. Introduction

Magnetic reconnection is a process where stored magnetic energy is converted into kinetic and thermal plasma energy. This energy conversion is caused by a macroscopic change in the magnetic topology. How this process evolves is highly dependent on the conditions of the magnetic fields and plasma in which it occurs. Significant multiscale differences in configuration, evolution, and efficiency of the reconnection process have been shown to depend on both the initial symmetry, shear and magnitudes of the magnetic field, and the temperature, composition, distribution, and dynamics of the plasma (Dargent et al., 2019, 2017; Pritchett & Coroniti, 2004; Swisdak et al., 2003; Tenfjord et al., 2018, 2020; Toledo-Redondo et al., 2021).

Magnetic reconnection can occur in many different locations in our magnetosphere, but the two main types of reconnection are dayside and nightside reconnection. In general, nightside reconnection is more symmetric, while dayside reconnection happens between very different plasma regimes, including strong gradients in particle density, temperature, magnetic field strength, and different magnetic shear. Both dayside and nightside reconnection have been modeled and observed extensively in the last couple of decades, with great strides being made in our observational capabilities since the launch of the magnetospheric multiscale (MMS) mission in 2015 (Burch & Phan, 2016).

In dayside reconnection, the magnetic field of the Earth connects directly with the interplanetary magnetic field (IMF) carried by the solar wind. From theory, large scale modeling, and observations we know that the direction of the IMF relative to the magnetic field of the Earth is crucial in determining how their interaction will occur (Fuselier et al., 2011; Trattner et al., 2017, 2007). In most cases of dayside reconnection, Earth's planetary and the IMF are not strictly antiparallel, meaning that the reconnecting fields are only the components of the total fields that happen to be antiparallel. During such guide field or component magnetic reconnection, the dynamics and global behavior of the reconnection process is modified on all scales compared to the strictly antiparallel

scheme. The addition of a guide field alters the kinetic behavior of the particles in the diffusion region (Goldman et al., 2011; Pritchett & Mozer, 2009) and the global configuration and efficiency of reconnection as a whole (Pritchett, 2005; Pritchett & Coroniti, 2004; Swisdak et al., 2005; Trattner et al., 2017).

Great progress has been made toward understanding symmetric, asymmetric, and guide field magnetic reconnection, both through modeling and observations (e.g., Burch et al., 2016; Cassak & Fuselier, 2016; Chen et al., 2017; Fuselier et al., 2017; Hesse et al., 2016, 2021; Torbert et al., 2018; Wilder et al., 2018). Several simulation studies compare how similar reconnection schemes are modified by changing one or more of the initial conditions (Dargent et al., 2020; Kolstø et al., 2020a, 2020b; Spinnangr et al., 2021; Tenfjord et al., 2019, 2020). As the Sun, the solar wind and the magnetosheath are highly dynamic, it is of great importance to understand how a reconnecting system responds to variations in the inflow conditions, in particular for dayside reconnection. Scenarios such as variations in the IMF, flux rope coalescence (Akhavan-Tafti et al., 2020, 2019; Zhou et al., 2017), and re-reconnection (Poh et al., 2019) can all give rise to reconnection events where the inflow magnetic shear angle varies. With this in mind, we employ in this study 2.5D fully kinetic particle-in-cell (PIC) simulations to investigate how the transition between different inflow conditions occur, by imposing asymmetric variations in the inflow magnetic field during one simulation of a reconnection event. By effectively turning on and off a guide field in one of the inflow regions by rotating the magnetic field into the out-of-plane direction, we find variations in both large and small scale dynamics of the system.

The reconnection rate shows significant temporal variations associated with the transient field variations. Consequently, the system is prevented from settling to a quasi-steady state through almost the full simulation time. We find that the variations in the reconnection rate cannot be fully explained by common scaling schemes such as the symmetric Sweet-Parker (Cassak et al., 2017; Comisso & Bhattacharjee, 2016; Y. H. Liu et al., 2017) or general Cassak and Shay (2007) scaling. In particular, we find that nonlinear effects become important, as changes in the reconnection rate precede changes in the inflow, leading to overshoots in the rate. As the rate varies, so does the flux transport into and out of the reconnection site. We also identify large scale structures in the exhaust that can act as signatures of varying inflow conditions, which are very different from the otherwise laminar exhaust of normal, antisymmetric reconnection.

The structure of the article is as follows: In Section 2, we describe the simulation setup we have employed in this study. In Section 3, we investigate how the reconnection rate varies with the variations in the inflow. Section 4 is a closer investigation of the flux transport into the reconnection site, while, in Section 5, we investigate how the exhaust responds to the inflow variations. Section 6 is a summary of our results with some discussion.

2. Simulation Setup

We utilize two fully kinetic, 2.5D PIC simulations, both based on the code described by Hesse et al. (1999), initializing a Harris current sheet of half-width $l = 1\ d_i$. Lengths are normalized to the ion inertial length, $d_i = \frac{c}{\omega_{pi}}$, where $\omega_{pi} = \sqrt{\frac{n_0 e^2}{\epsilon_0 m_i}}$ is the ion plasma frequency with n_0 being the initial Harris current sheet density and m_i is the ion mass. Time is normalized to the inverse ion cyclotron frequency, $\Omega_i^{-1} = \frac{m_i}{eB_0}$, where B_0 is the initial asymptotic magnetic field, and we employ a time step of $\omega_{pe}\delta t = 0.5$. Densities are normalized to n_0, and velocities are normalized to the ion Alfvén velocity, $v_A = B_0/\sqrt{\mu_0 m_i n_0}$. A highly localized perturbation is employed, initializing the magnetic reconnection process. In our coordinate system, x is the reconnection outflow direction, y is the initial current direction, and z is the inflow direction. The boundary conditions are periodic in the x-direction and specular reflection in the z-direction. We use a total of 1×10^9 macro-particles, and the size of the simulation domain is $204\ d_i \times 102\ d_i$ divided into a grid of $3{,}200 \times 3{,}200$ cells. The ions and electrons have a mass ratio of $\frac{m_i}{m_e} = 25$ and their temperature ratio is $\frac{T_e}{T_i} = 0.2$. The ratio of the ion plasma frequency to the electron cyclotron frequency is $\omega_{pe}/\Omega_e = 2$.

We refer to the two simulations as the baseline run and the varying run, where the varying run includes an asymmetric, varying magnetic field contribution in the y-direction with associated current modifications, but is otherwise identical to the baseline. Our initial magnetic field configuration is:

$$B_x = B_0 \tanh(z/l)\ \ f(z) \tag{1}$$

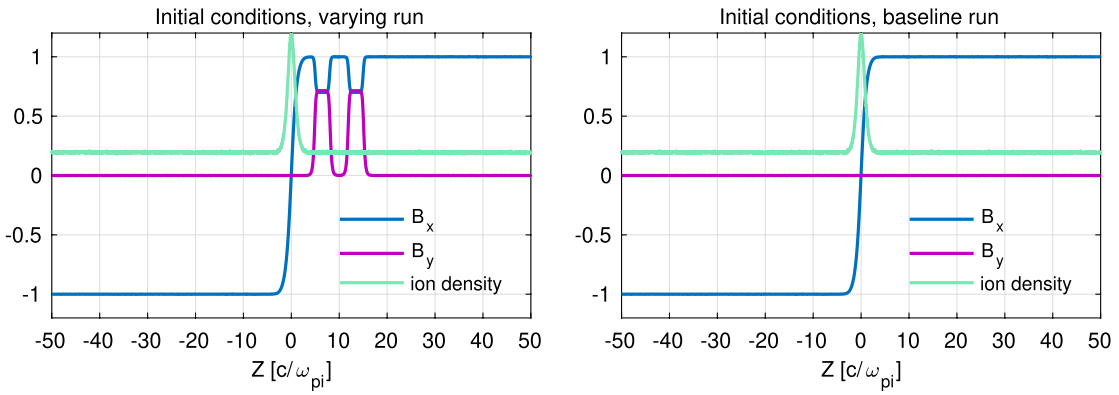

Figure 1. Cut along Z through the center of the box showing the initial values of the magnetic fields and the ion density for the varying run (left) and the baseline run (right). The total magnitude of the magnetic field ($B = \sqrt{B_x^2 + B_y^2}$) is the same in both runs.

$$f(z) = 1 + \alpha \sum_{j=1}^{4} (-1)^j \left(1 + \tanh\left(\frac{z - z_j}{\lambda}\right)\right) \tag{2}$$

$$B_y = \sqrt{\tanh^2(z/l) - B_x^2} \tag{3}$$

The function f modifies the magnetic field direction, effectively turning on and off the guide field. The factor z_j in $f(z)$ specifies the locations in the inflow regions where the field direction changes, which we have set as [5 7.5 10 12.5]d_i, creating two horizontal bands of positive B_y in the inflow region above the current sheet. The factors $\alpha = 0.15$ and $\lambda = 0.25$ d_i serve to modify the magnitude and steepness of the variation, respectively. When $|z - z_j|$ is large, $f = 1$, which is the case everywhere for the baseline run where Equations 1 and 3 reduce to the normal Harris configuration. Our magnetic field configuration ensures that the magnitude of the total magnetic field stays constant when the field changes direction. Hence, only the magnetic field components change, while the total magnetic energy density remains the same. Figure 1 shows the initial values of the magnetic field profile and the ion density for both runs. In Figure 2, we give an overview of the time evolution of the y-directed magnetic field for both runs and the total y-directed current for the varying run. In the first panel of the middle column, we label different regions of the inflow that will propagate through the simulation. We will continue to use these labels for referencing throughout the text.

3. The Reconnection Rate

The reconnection rate tells us how fast the reconnecting system is able to convert magnetic energy into plasma kinetic and thermal energy, and therefore says something about how effective the reconnection process is. In Figure 3, we show the amount of reconnected flux, Φ, and the reconnection rate, $d\Phi/dt$, as functions of time. By looking at the reconnected flux, we see that the baseline reconnects more efficiently, and has converted about 12% more magnetic energy in the same amount of time compared to the varying run at the end of the runs. Based on earlier studies, this is about the same reduction we could expect from introducing a uniform guide field in the whole box (Huba, 2005; Ricci et al., 2004; Swisdak et al., 2005).

When we compare the reconnection rates, we see that the two runs behave very similarly until they start to deviate significantly around $t = 40$. The baseline run exhibits the expected behavior, with a fast increase in the rate followed by a slow and steady decline as the amount of magnetic energy available in the system is being depleted. The varying run on the other hand, shows significant variations in the rate, which coincide with the varying inflow conditions. As a first step in analyzing these variations, we develop a scaling relation based on the reconnection rate scaling for asymmetric reconnection developed by Cassak and Shay (2007). They find a general expression for the reconnection electric field in an asymmetric configuration:

$$E \sim \left(\frac{B_1 B_2}{B_2 + B_1}\right) v_{out} \frac{2\delta}{L} \tag{4}$$

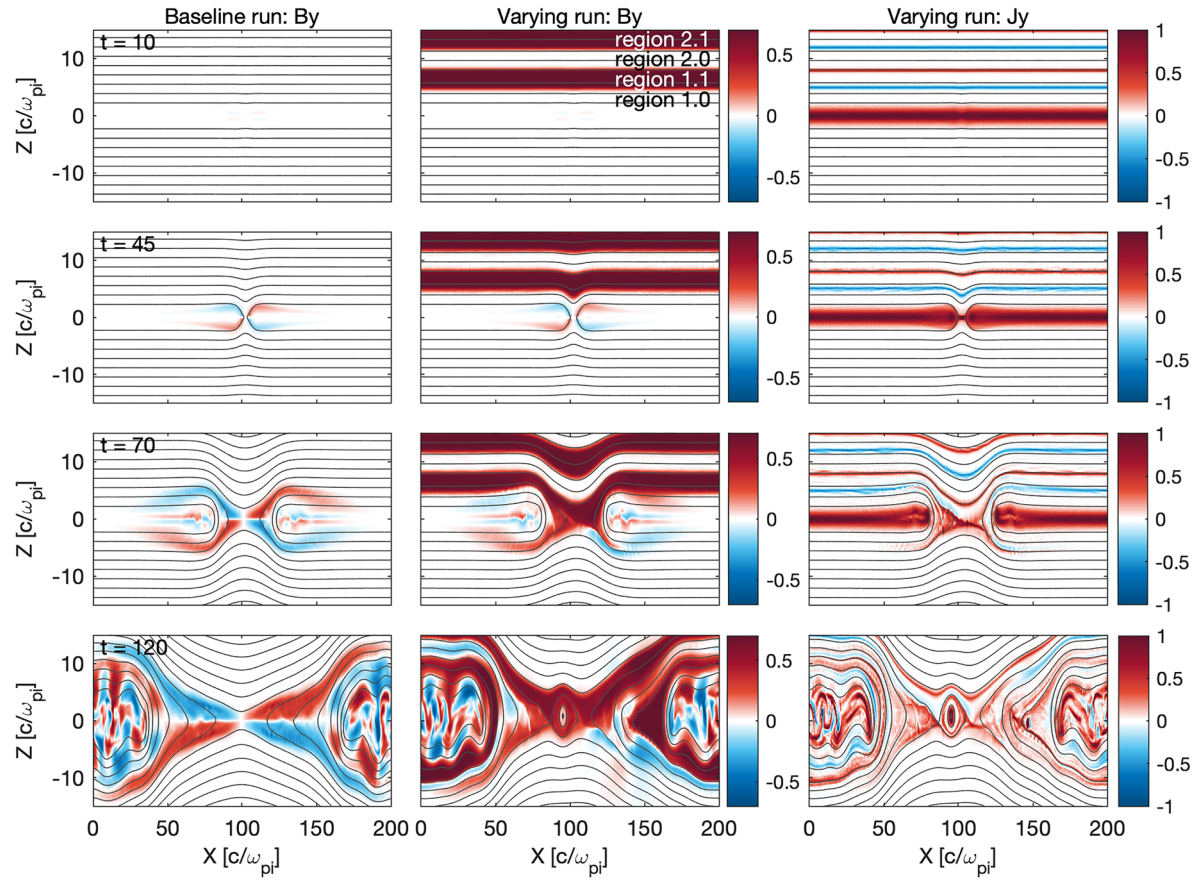

Figure 2. Overview of the evolution of the *y*-directed magnetic field in the two runs, as well as the *y*-directed current in the varying run. The contours show the in-plane magnetic field. We have labeled the regions of different magnetic field configurations in the top inflow region to refer to them more easily in the analysis later. When the decimal is 0, the B_y is also 0.

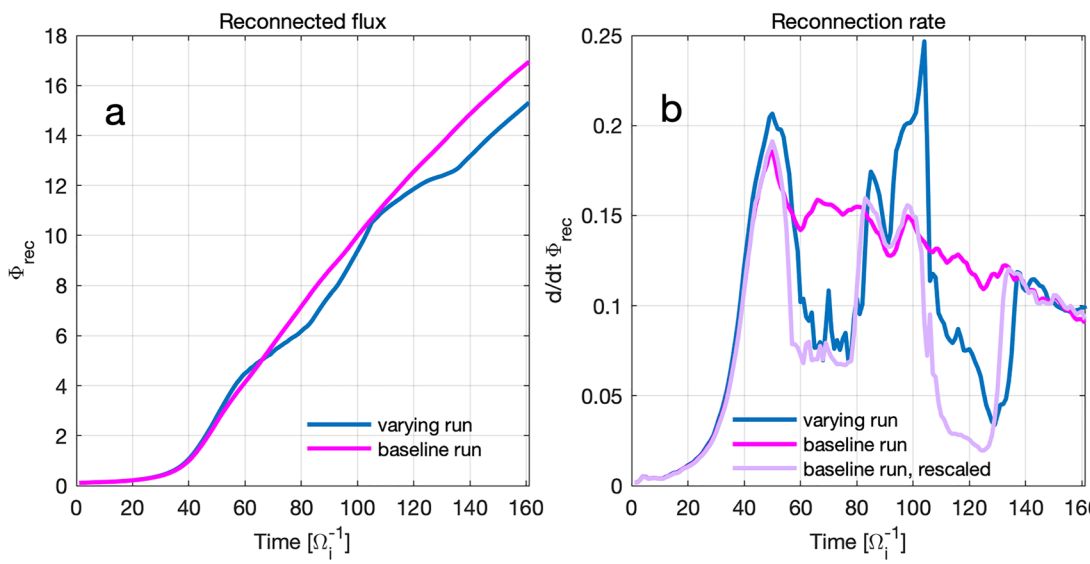

Figure 3. Panel (a) shows the total amount of reconnected flux as a function of time for the two runs. Panel (b) shows the reconnection rate as a function of time for the two runs, as well as the baseline run rescaled to the variations in the inflow magnetic field, as described in the text.

where B_1 and B_2 are the asymmetric magnetic field magnitudes in the inflow regions, v_{out} is the outflow speed, and $\frac{\delta}{L}$ is the aspect ratio of the diffusion region. They also find a general expression for the outflow speed, which in our runs reduces to:

$$v_{out}^2 \sim \frac{B_1 B_2}{\rho} \tag{5}$$

Here, we use their expressions for a symmetric density distribution. In the baseline run, the density is symmetric, while in the varying run some small asymmetries develop during the course of the run. The ρ we use in Equation 5 for the varying run is the average ρ above and below the current sheet. The ratio of the density difference between the two inflow regions to this average density is small compared to the corresponding ratio for the magnetic field, $(\rho_1 - \rho_2)/\langle\rho\rangle \lesssim 0.25$ while $(B_1 - B_2)/\langle B\rangle \sim 0.8$–$1.2$, and we ignore them in this analysis. Equations 4 and 5 can be interpreted as the reconnection electric field and the outflow velocity based on the effective magnetic field in the inflow, respectively.

Dividing Equation 4 for the varying run, E_v, by that for the baseline run, E_b, we find a scaling factor for the reconnection electric field:

$$\frac{E_v}{E_b} \sim \frac{\frac{B_1 B_2}{B_1 + B_2}}{B} \frac{\sqrt{\frac{B_1 B_2}{\rho}}}{\frac{B}{\sqrt{\rho}}} \frac{2\frac{\delta}{L}}{\frac{\delta}{L}} = \frac{2(B_1 B_2)^{\frac{3}{2}}}{B^2(B_1 + B_2)} \tag{6}$$

The magnetic field below the current sheet in the varying run, B_2, behaves in the same way as the baseline magnetic field, B, ($|B - B_2| \lesssim 0.2$), so we can set $B_2 = B$ in Equation 6, which then reduces to:

$$\frac{E_v}{E_b} \sim \frac{2(B_1)^{\frac{3}{2}}}{\sqrt{B_2}(B_1 + B_2)} \tag{7}$$

The right hand side of Equation 7 is now a scaling factor, only dependent on the magnetic field strengths, which we can use to compare the reconnection rate in our varying run with what has been reported for constant (or global) asymmetric configurations. In Figure 3b, we have plotted the baseline run rescaled with this factor together with the original rates from the two runs. The slight shift in time between the variations in the guide field rate and the rescaled baseline rate happens because we pick values for B_1 and B_2 1 d_i away from the X-point, meaning the scaling factor uses a reduced field strength before it actually arrives at the reconnection site. We see that by rescaling the baseline with the magnetic field variations in the varying run, we capture some of the overall behavior observed in the varying run, but there are still major differences between the rescaled baseline run and the varying run. Most notably, we see that the rescaling does not capture the overshoots in the rate occurring around $t = 50$ and $t = 100$ in the varying run. Also, for the second rate reduction between $t = 110$ and 135, the rescaling predicts a much larger rate reduction than the actual rate observed in the varying run. These differences indicate that there are important dynamics other than just the imposed field variations that dictate the behavior of the reconnecting system.

We can also use Equations 4 and 5 directly to estimate the reconnection rates based on the inflow conditions. In Figure 4, we have plotted the reconnection rates of the two runs, calculated using two different methods. The magenta and blue lines show the rates calculated based on the reconnection electric field for the baseline and the varying run respectively. These are the same rates as in Figure 3b. The turquoise lines in Figure 4 show the rates calculated using Equations 4 and 5 directly, with values for the magnetic field and density taken at $Z = \pm 3$ above and below the X-point, and assuming $\frac{\delta}{L} = 0.1$. Again, we see the large reductions in the rate are captured and to some degree overestimated, while the overshoots are not captured at all. The large difference between the rates before about $t = 40$ is artificial, as Equation 4 cannot give the correct rate before reconnection is ongoing. The larger delay between the two calculation methods compared to the delay when we do the scaling occurs because we must extract the relevant values further away from the current sheet when we apply Equation 4 directly, in order for expressions to be applicable. Closer to the X-point, the magnetic field strength is reduced, and using these values in Equation 4 therefore significantly underestimates the rates, while in the scaling it only modifies the actual rate, so the magnitude is not significantly affected by where we extract the values. The choice of aspect

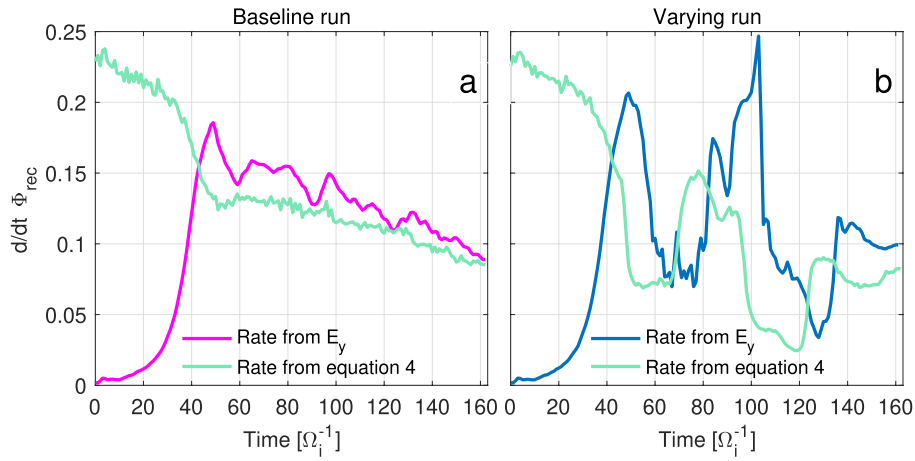

Figure 4. Comparison of the reconnection rates calculated using the reconnection electric field (E_y) and Equation 4. The values of the magnetic field and density needed in Equation 4 were taken at $Z = 3\ d_i$, which explains the offset in timing of the variations in the varying run.

ratio = 0.1 has been shown to be a reasonable value in many different reconnection configurations (Cassak et al., 2017; Comisso & Bhattacharjee, 2016).

The scaling of the reconnection rate presumes a quasi-steady state, and as we will see in the next section, our system is not quasi-steady until the variations in the inflow have convected downstream of the X-point. Since the reconnection rate is a measure of how efficiently the reconnection process converts magnetic flux, it says something about how efficiently the flux is transported into and out of the reconnection region. This means that the system must somehow adjust the flux transport into the reconnection site in response to the variations in the magnetic field. We will analyze this further in the next section.

4. Flux Transport Analysis

In the previous section, we saw that the reconnection rate is significantly affected by the varying inflow conditions, but not in a manner that is consistent with the magnetic field configurations alone. In this section, we investigate more closely how the reconnecting system readjusts itself to the variations in the inflowing magnetic field. In Figure 5, we show the evolution of B_y, $|B_x|$, the ion $|v_z|$ and density n, and E_y as a function of time, together with the reconnection rate. To construct these plots, we have taken slices along z through the X-point for every time step of the simulation, and then plotted these slices consecutively with time on the x-axis. All the variables in each slice are averaged over a distance 0.1 d_i to both sides of the X-point to reduce noise. The dark gray lines in panels a through e are lines of constant values of the magnetic vector potential, **A**, defined by $\mathbf{B} = \nabla \times \mathbf{A}$. We construct these lines by extracting values of **A** for each time step along the same slices as described above. They indicate the motion of given magnetic fields lines in the inflow region. The black line around $z = 0$, where the gray lines converge, is the position of the dominant X-point.

In Figures 5a and 5b, the regions where the direction of the magnetic field is turned toward the y-direction are seen as bands of enhanced and decreased magnitudes of B_y and B_x respectively, that move in toward the reconnection site as time progresses. These bands correspond to the initial bands of magnetic field labeled regions 1.1 and region 2.1 ($B_y = B_x = 0.7$) in Figure 2, while the regions inside and between the two bands correspond to region 1.0 and 2.0 ($B_y = 0$). In Figure 5c, we see that as regions 1.1 and 2.1 move toward the reconnection site (from around $t = 48$ and $t = 93$), a significant asymmetric increase in the inflow velocity occurs. This is the case for both regions, but it is especially apparent for region 2.1. The change in inflow velocity somewhat precedes the change in the magnetic field, evident from the fact that the velocity asymmetry both builds up and recedes before the equivalent change in the magnetic field arrives at the X-point.

We can explain this behavior and the offset in timing between the changes in the inflow velocity and the magnetic field by force balance arguments. The inflow velocity is to a large degree determined by how quickly the reconnection process convects the plasma out in the exhausts. To maintain pressure balance, the inflowing plasma is

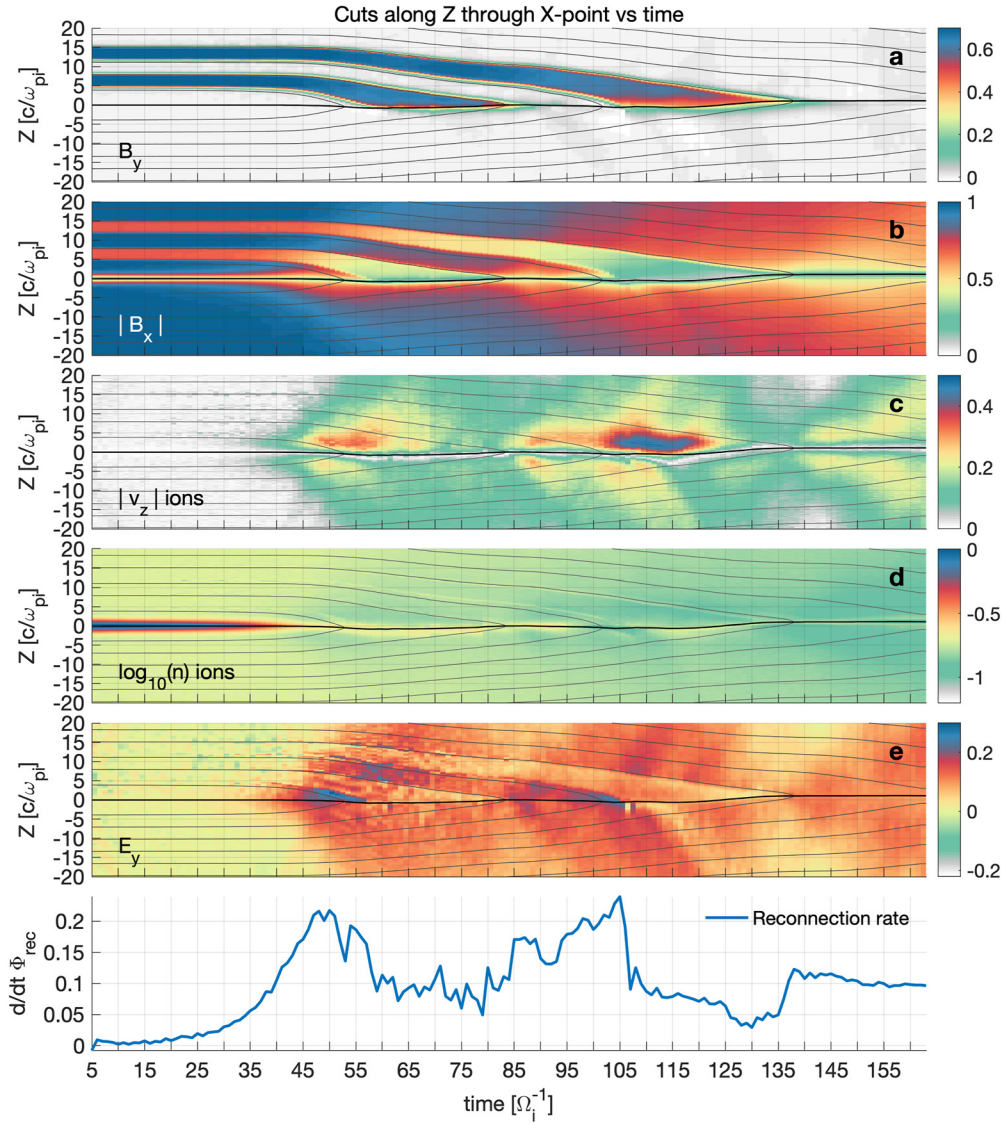

Figure 5. Temporal evolution of inflow regions. Panels (a) through (e) shows cuts through the dominating X-point along the z-direction, each cut plotted as a function of time (see text for detailed description of plot construction). The dark gray lines in panels (a) through (e) are lines of constant values of **A**, and the black line along the center shows the position of the X-point. Panel (a) shows B_y, panel (b) shows the magnitude of B_x. In both, we see regions 1.1 and 2.1 presented as bands of different field strength moving toward the X-point as time progresses. Panel (c) shows the magnitude of the ion inflow velocity, panel (d) shows the ion density in log scale, panel (e) shows the reconnection electric field, and the last panel shows the reconnection rate.

heated to balance the pressure loss from convection to the outflow. If the convection of pressure out of the central region is not balanced by transport of plasma in the inflow, Alfvén waves are launched to adjust the inflow appropriately and vice versa, that is, the inflow and outflow are not independent of each other. In Figure 5d, we see that the initial current sheet density has already been convected into the exhaust around $t = 40$, before the changes in magnetic field start to interact with the reconnection process. The transport of the reconnection magnetic field component, B_x toward the X-point is governed by the strength of the field and the speed at which it is transported. Since B_x is lower in regions 1.1 and 2.1, the system must readjust itself to ensure that the flux is convected equally from the top and the bottom inflow.

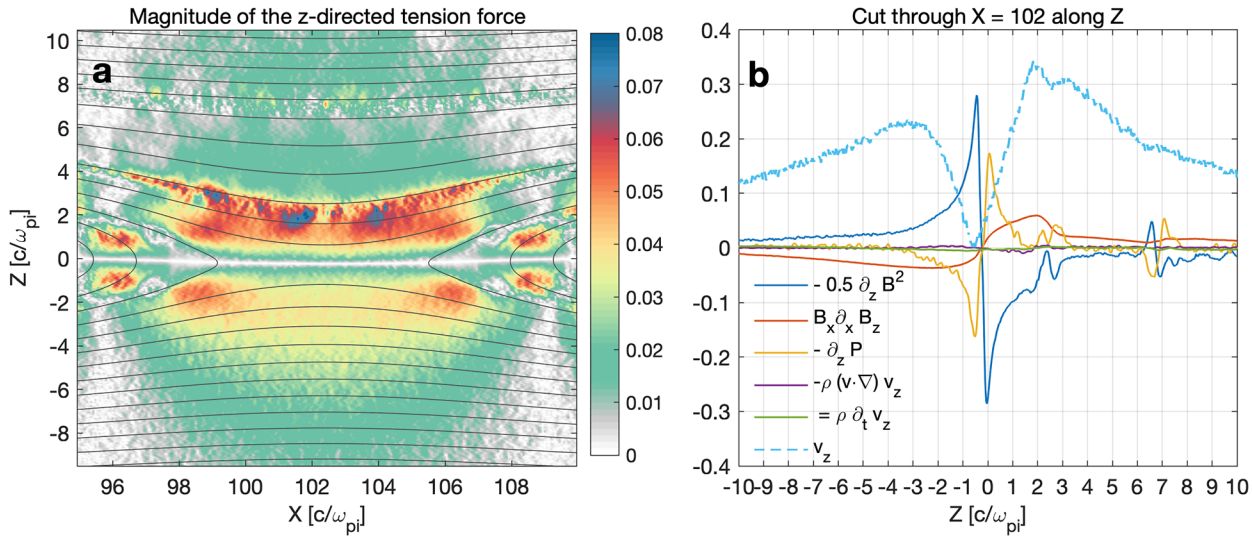

Figure 6. Panel (a) shows a map of the magnitude of the z-directed tension force around the reconnection site, with contours of the in-plane magnetic field. Notice region 1.1 between about $Z = 3$ and $Z = 7$, where the magnitude of the in-plane magnetic field is smaller, as indicated by the larger spacing between the contour lines. Panel (b) shows a cut along the z-direction through $X = 102$ of all the terms in Equation 8. The red line is the tension force, and the cyan dotted line is the inflow velocity. The purple and green lines are the inertia contributions, which we see are negligible. Both panels are for $t = 50$, corresponding to the time of the first peak reconnection rate.

The changes in the inflow velocity when region 1.1 approaches the reconnection site can be understood by looking at the balance between the magnetic forces and the thermal pressure force. These forces can be expressed through the total momentum equation as:

$$\rho\left(\frac{\partial v_z}{\partial t} + v_z\frac{\partial \vec{v}}{\partial z}\right) \sim 0 \quad = \quad \left(\vec{J}\times\vec{B} - \nabla P\right)\Big|_z \\ = \quad -\frac{\partial}{\partial z}\left(\frac{1}{2}B^2 + P\right) + B_x\frac{\partial B_z}{\partial x} \tag{8}$$

where ρ is the ion mass density, v is the ion velocity, B is the magnetic field and P is the plasma pressure. As we will show later, the inertia terms are small and can be neglected in the following analysis. The first and second terms of the second line represents the magnetic and thermal pressures, respectively. The last term represents the magnetic tension, which becomes important as the field lines expands toward the diffusion region. Since the tension force is proportional to B_x, the reduction of B_x inside regions 1.1 and 2.1 leads to a top-bottom asymmetry in the magnetic tension force. To intuitively understand the overshoot (and undershoot) of the reconnection rate described in the previous section, as well as the motion of the X-point which we discuss later in this section, we consider the variation in this tension term, both in its total magnitude and in the distribution between the two factors.

The initial conditions are a Harris sheet configuration with varying guide field, where the thermal and magnetic pressure are in balance. Once reconnection starts, and magnetic flux is convected toward the X-point, the field starts to deform, generating a gradient in B_z along the x-direction as it expands, giving rise to a tension force. Before region 1.1 gets involved in the reconnection process, that is, until approximately $t = 45$, the tension on the two sides is approximately symmetric.

When region 1.1 approaches the diffusion region, the symmetry of the tension force above and below the current sheet breaks down. To understand how the system reconfigures to accommodate the spatially asymmetric tension we look at the momentum equation along a cut through $X = 102$ along the z-direction. Figure 6a shows a map of the magnitude of the z-directed tension force, and Figure 6b shows the components of Equation 8, both at $t = 50$. The dark gray lines in the map are contour lines of the in-plane magnetic field. We can see the location of region 1.1 in the inflow where the spacing between the contour lines is larger, approximately between $z = 3\ d_i$ and $z = 7\ d_i$. There is a clear asymmetry in the tension force above and below the current sheet. The tension force is reduced in region 1.1 ($z \gtrsim 3\ d_i$) compared to the corresponding distance from the X-point in the bottom inflow region

($z \lesssim -3$). However, closer to the reconnection site, $0.5 < |z| < 3$, the tension is stronger in the top inflow. This is also seen in Figure 6b (red line) where the tension is stronger for the top side close to the reconnection site, but is clearly reduced in region 1.1 ($z > 2.5\ d_i$).

The reduced tension in region 1.1 allows the region to expand, which exerts a larger pressure force on the inner region (1.0). Region 1.0 is thus compressed, leading to a higher magnetic pressure and tension force in this region. The effect of this is an increase in v_z in the top inflow, as seen in Figure 6b (dotted line). As a consequence of the enhanced v_z, the flux tubes ahead of the region of reduced tension are deformed further, as they experience a higher local transport toward the reconnection site. During this equilibration process, the current sheet is moved slightly downwards, as can be seen in the black line in Figure 5.

The thermal and magnetic pressure forces also respond to the dynamics induced by the tension force, seen in Figure 6b between $z = 2$ and $z = 3\ d_i$. The expansion of the regions of lower tension force is also what facilitates the nonlinearity of the reconnection rate variations we observed in the previous section. Since the field deformation is not confined to the regions 1.1 and 2.1 of sheared magnetic field (finite B_y), the increased inflow velocity and its effect on the flux transport can reach the X-point before regions 1.1 and 2.1. This leads to the overshoots in the rate around $t = 50$ and $t = 105$ and explains why the rate does not drop as low as the scaling with the magnetic field magnitudes predicted for $t = 60$–80 and $t = 110$–130, the so called undershoots.

The detailed analysis of the flux transport in this section was motivated by the dynamics of the reconnection rate we presented in the previous section. It was clear that the rate variations could not be explained by the magnitude of the reconnecting field component alone (Equation 7). In Figure 5e, we see variations in the strength of E_y that are associated with the variations in the inflow velocity and the B_x component. At the times of the overshoots in the reconnection rate ($t = 50$ and $t = 105$), we see clear, continuous enhancements in the strength of E_y a few d_i away from the X-point in the top inflow. As regions 1.1 and 2.1 reache the X-point, the reduction of the B_x component is large enough that the E_y and the reconnection rate are reduced, but by the same argument, the increased v_z makes this reduction less than it would have been if the inflow velocity remained the same.

We have seen in this analysis of the inflow that asymmetries in the magnetic tension force facilitate an increased inflow velocity from the top inflow region. By the same arguments, we can describe how the X-point moves back up to its original equilibrium position when reconnecting region 2.0 and after reconnecting region 2.1. We see this happening in Figure 5 between $t = 60$ and $t = 80$, and $t = 115$ and $t = 130$. The system finally settles in a quasi-steady state as region 2.1 is convected into the outflow and the inflow becomes symmetric once again, from about $t = 140$ and onwards. This simulation also emphasizes that a quasi-steady-state is not achieved immediately, and signatures of the reconfiguration are present during a significant portion of the simulation time. The different regions of magnetic shear in the inflow region are convected into the reconnection site with a velocity defined by the flux transport, which we have seen varies. Nevertheless, the transition between the two shear configurations happen over about 3–4 ion cyclotron times, and each configuration phase at the x-point lasts for about 10–30 ion cyclotron times, as can be seen in Figure 5. If we assume a magnetic field strength of 20 nT, which is typical for the dayside magnetosheath (Toledo-Redondo et al., 2021), one ion cyclotron time corresponds to 3 s. The turning of the magnetic field in this simulation therefore occurs in about 10 s, and the duration of each configuration phase at the reconnection site is in the order of one minute. In the next section, we will see that the modulations to the reconnection rate caused by non-steady inflow conditions are also manifested in the outflow magnetic and electric fields.

5. Exhaust Structure

As discussed in the previous section, the behavior of the inflow and the outflow are interconnected, and it is therefore natural to assume that the variations in the inflow will affect the outflow. In Figure 7, we have plotted variables in the outflow using the same approach as in Figure 5. Here, the slices are taken along the x-direction through $z = 0$ instead of following the X-point along the z-direction. As we saw in the previous section, the X-point does move up and down during the reconnection process. We still chose to cut through $z = 0$ as the effect of this vertical movement is more local in and around the diffusion region, while in this analysis we will investigate general features further out in the outflow that are unaffected by this dynamic. From the top to bottom in Figure 7, we show B_y and B_z, the electron outflow velocities v_x and v_y, the ion density and the reconnection electric

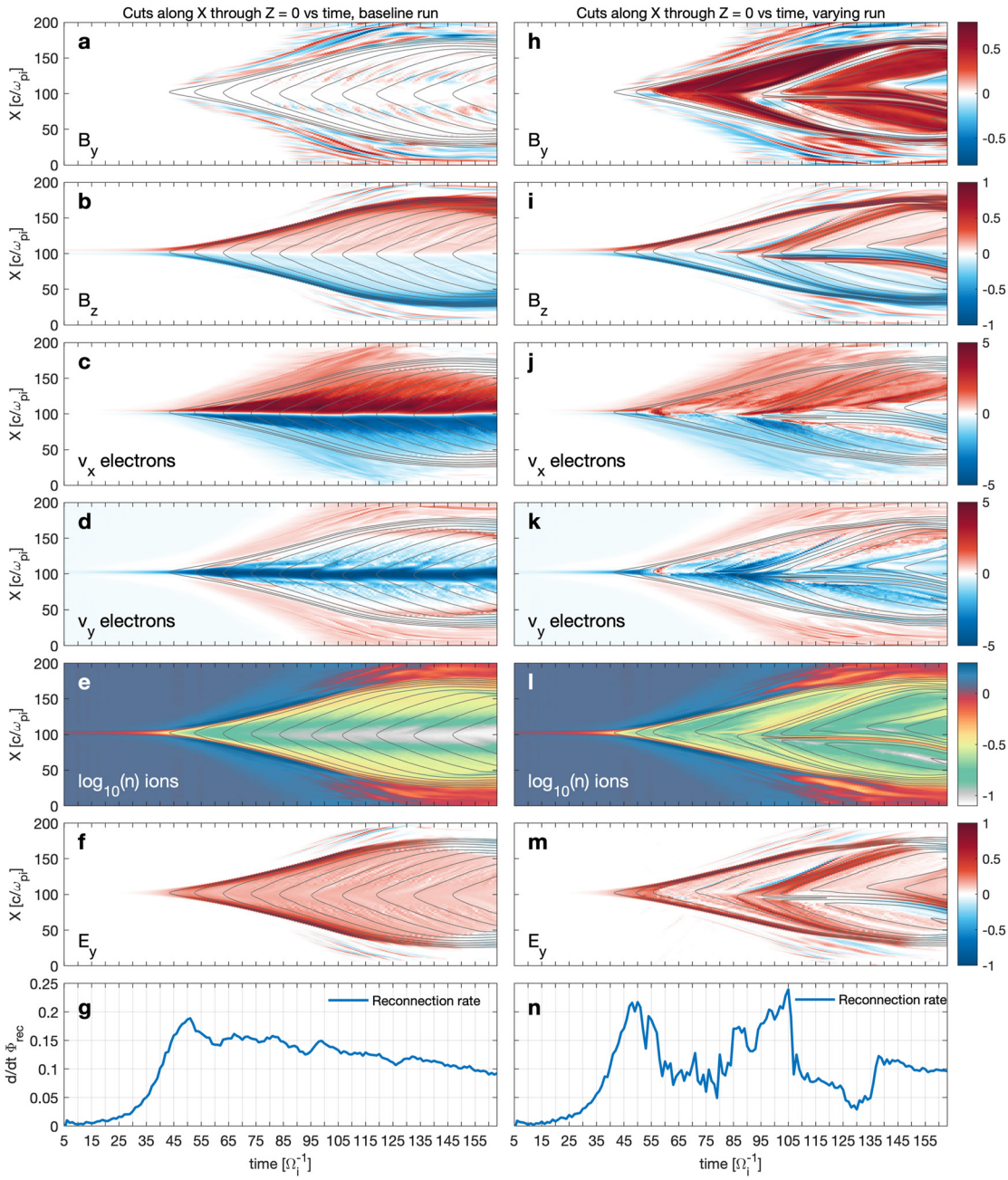

Figure 7. Cuts through $z = 0$ along the x-direction, plotted as a function of time (see text for detailed description of plot construction). Panels (a) through (g) are the baseline run, panels (h) through (n) are the varying run. The dark gray lines in panels showing a color map are lines of constant values of the magnetic field vector potential, **A**. Panels (a and h), and (b and i) show the y and z-directed magnetic field, panels (c and j), and (d and k) show the x and y-directed electron velocities, panels (e and l) show the ion density in log scale, panels (f and m) show the reconnection electric field, and panels (g and n) show the reconnection rates.

field, E_y, ending with the reconnection rate. The panels in the left column show the variables for the baseline run, while the ones in the right column are the varying run.

Looking at the panels in the baseline column, we see that the baseline run evolves smoothly, with a laminar outflow. The magnetic and electric fields are generated and convected symmetrically in both directions along x, and the initial current sheet is convected away smoothly. The electron velocities show well defined enhancements in both the x- and y-direction close to the middle of the x-axis. The enhancement in the v_{ex} corresponds to the embedded electron jet caused by the meandering motions of the electrons (Drake et al., 2008; Shuster et al., 2015;

Tenfjord et al., 2020). Just by a quick glance at the column showing the varying run it is easy to see that the varying inflow conditions have an impact on the structure of the outflow, making it significantly less laminar. We see clear signatures associated with the varying guide field that appear at the X-point and propagate downstream. With the exception of the initial pile-up of magnetic field B_z, and corresponding flux, that forms at round $t = 50$, these structures are not present at all in the baseline run. In both the magnetic and electric fields, as well as in the ion density, we see well defined regions where the B_y component is being convected. We saw in the previous section that regions 1.1 and 2.1 become broader in time as they approach the X-point in the inflow when the flux transport is slower. We see the same broadening of these regions in the outflow in Figure 7h. Where there is no B_y, we see enhancements in both the B_z component, the reconnection electric field and the ion density. Although the density was initially uniform and symmetric between the two inflow regions, the variations introduced by the varying inflow magnetic field leads to density variations in the outflow. For both runs, the first region of enhanced B_z is associated with a density decrease. This density decrease is related to the decrease in the inflow density seen in Figure 5d. In contrast, the following flux pile-up region in the run with varying guide fields, forming at around $t = 85$–105, is associated with a density increase.

By considering the timing of their appearance in the outflow and their behavior as collective structures, in addition to their absence in the baseline run, we suggest that these transient structures in the outflow are formed as a consequence of the varying inflow conditions. An important implication of this is that structures originating in the inflow survive the reconnection process and are convected out in the outflow. This means that structured, nonlaminar outflows can be a consequence of the inflow conditions rather than the result of kinetic dynamics in the diffusion region. Such structures in the outflow may therefore be useful to infer the inflow conditions necessary to create them. Observations of large scale variations in the outflow can be a direct consequence of varying inflow conditions. However, the variations in the outflow can also be formed as an indirect consequence of the inflow variations, by the means of reconnection rate changes. The variation in B_z is one example of this. A higher reconnection rate means more flux transport in the outflow, while a lower rate leads to slower transport of B_z flux. These variations in formation rate and propagation speed of B_z lead to the formation of flux pile-up regions where the magnitude of B_z is enhanced, when fast moving field lines catch up with slower moving field lines (Norgren et al., 2021). In Figure 7, we can see that the flux pile-up regions form during times of increased reconnection rate. Since we have shown that the reconnection rate variations are caused by the variations of the inflow guide field, we also conclude that secondary flux pile-up region in the run with varying guide field is a result of the varying guide field. In extension, we would also expect that similar B_z variations in the outflow form in systems with a reconnection rate that varies due to other factors in the inflow or the diffusion region.

We also see differences in the electron dynamics between the two runs. Figures 7c and 7d show the electron outflow velocities, v_{ex} and v_{ey}, respectively, for the baseline run, while Figures 7j and 7k show the same for the varying run. In the varying run, we have a significantly reduced outflow speed compared to the baseline run. Both v_{ex} and v_{ey} in the varying run are also significantly more structured compared to the laminar outflow in the baseline, exhibiting regions of electrons flowing in the opposite direction and with a lot of small scale structures of different velocity magnitudes. Comparing Figures 7c and 7j, we clearly see the embedded electron jets close to the X-point in the baseline run, while they are not distinct in the varying run. The electron jets associated with antiparallel symmetric reconnection with uniform inflow have been observed (Phan et al., 2007) and modeled (Hesse et al., 2008) to be faster than the $\vec{E} \times \vec{B}$ drift, suggesting that the jetting electrons are demagnetized. When reconnecting regions 1.0 and 2.0, we see an increase of the v_{ex} close to the X-point, but this feature is destroyed when reconnecting regions 1.1 and 2.1. This is consistent with earlier studies of electron dynamics during guide field reconnection, where it has been shown that a guide field will deflect the x-directed electrons along the separatrices (Goldman et al., 2011). The regions of increased and decreased v_{ex} magnitude close to the X-point in Figure 7j are therefore signatures of the system transitioning between the normal electron jet and the deflected electron flow respectively, in response to the variations in the magnetic field direction.

In addition to the various transient structures either directly associated with the convection of the B_y magnetic field through the outflow and/or the variations in the reconnection rate, we also see a much higher rate of island production in the varying run. One large island forming around time = 95 is clearly visible as it travels toward smaller x (downwards in Figure 7), but at least four smaller islands form during the simulation. It is possible that the formation of multiple islands is a consequence of the many reconfiguration iterations the system undergoes in response to the imposed variations in the inflow magnetic field. Variations in the reconnection rate, motion of

the reconnection site, and various asymmetries could all conspire to facilitate a higher rate of island production, which also makes the outflow in general more structured. The mere presence of a guide field will also cause the system to generate secondary islands at a higher rate than in a purely antiparallel scheme (Drake et al., 2006). We observe island generation while both regions with and without a guide field are reconnecting, but since these regions are fairly narrow, it is not possible to determine if it is the presence of a guide field alone or a synergy of it and its variations that generates the islands. The presence of secondary islands is also known to affect the reconnection rate (e.g., Cassak et al., 2017), and they are a likely cause of the smaller rate variations we see on top of the large scale behavior caused by the varying inflow conditions.

Typical values for the proton density in the magnetosheath are 15–20 cm^{-3} (Toledo-Redondo et al., 2021), making one ion inertial length in our simulations about 50–60 km. The larger scale structures we see in the magnetic and electric fields and the ion density vary in width between 10 and 30 d_i, meaning they are in the range of 500–1800 km wide. The smaller scale structures we see in the electron velocities and the ion density are just a few d_i wide, corresponding to a few hundreds of km.

6. Summary and Discussion

We have investigated how a system undergoing collisionless magnetic reconnection reacts to varying inflow conditions by asymmetrically varying the configuration of the magnetic field in the inflow region. We found that such variations have significant influence on both the larger and smaller scale dynamics of the reconnecting system, as we see correlated variations in the reconnection rate, the flux transport and the structure of the exhaust. To a large extent, the overall behavior of the reconnection rate was found to be dictated by the magnitude of the reconnecting component of the magnetic field, consistent with the general scaling developed by Cassak and Shay (2007). However, significant deviations from the behavior predicted by the scaling were also identified while reconnecting regions 1.1 and 2.1. We found that as the reconnecting components became asymmetric, the ion inflow velocity increased on the side where the reconnecting component was reduced. The increased inflow velocity reduces the effect of the lower magnitude of B_x on the reconnection rate by increasing the flux transport. This was possible because the magnetic tension force became asymmetric, being reduced in regions 1.1 and 2.1 as they approached the reconnection site, and increased right in front of the transition between regions with and without guide field. These dynamics caused z-directed convections of the reconnection site. In this study, we designed the simulation with varying guide fields on one side, similar to dayside reconnection with varying IMF. If the magnetic field variations were symmetric above and below the current sheet, the changes in velocity and flux transport would be the similar, but symmetric, and the X-point would not move.

We find the exhaust to be significantly less laminar when the inflow is varying, compared to a simulation with non-varying inflow conditions. Large scale structures of enhanced B_z, E_y, and ion density propagate through the exhaust. These structures form on flux tubes that had no B_y in the inflow. In the magnetotail, regions of magnetic flux pile up, often referred to as dipolarizing flux bundles (where the dipolarization front is the leading edge), are often associated with a decrease in the density (e.g., J. Liu et al., 2013). This anticorrelation between B_z and n was observed for the first flux pile-up regions in both the baseline and varying runs. In contrast, the second flux pile-up region observed in the run with varying guide field was associated with a density increase. This conjugate increase of B_z and n is a result of the compression of flux tubes and the associated plasma. We would expect similar plasma compression to be present also at the first pile-up regions. However, in these regions, the decrease in density due to inflow density variations is much larger, and compressional effects are negligible in comparison.

It is clear that the reconnection process does not act as a filter for the variations in the inflow region. The imposed guide field variations are carried through the diffusion region and convected through the exhaust, as seen in Figure 7h. The variations in the magnitude of the B_z component clearly coincide in time with the variations in the magnitudes of the inflow magnetic field. However, as we saw in Section 3, the reconnection rate shows significant variations in response to the varying inflow magnetic field. These variations in reconnection rate can lead to the formation of such structures of enhanced B_z, as discussed in Section 5. Although the B_z structures coincide with the regions of low B_y in the outflow, we cannot with certainty rule out that this may be a feature of the initial spacing of the B_y bands in the inflow. Other sources of a varying reconnection rate could lead to similar structures in the outflow B_z.

The x-directed electron flows close to the X-point seen in the baseline run are significantly reduced in the varying run while reconnecting the regions containing B_y. As discussed in Section 5, the absence of these flows is a result of the variation in the magnetic field direction. The guide field modifies the trajectory of the electron flow to be directed along the separatrices, that is, outside of the z-range we show in our plots. Additionally, smaller scale structures and variations in the magnitude of the outflow velocity in both directions are seen. The reconnection rate in the varying run is in general slightly lower than in the baseline run, consistent with a reduced outflow of flux, and less of the original current sheet is therefore seen to be convected away from the X-point in the varying run. Additionally, a much higher rate of island production contributes to make the varying run less laminar. Based on this, it is possible to argue that some variations and turbulence measured in the outflow are simply remnants of a fluctuating inflow, rather than a product of some kinetic dynamics in the diffusion region.

In summary, the varying guide field impacts the reconnection process in multiple ways, both directly and indirectly. Direct impacts include variations of the reconnection rate, transmission of the guide field to the exhaust and related modifications of the electron flows. Indirect impacts includes formation of multiple regions of magnetic flux pile-up in the exhaust that are associated with density increases, and nonlinear modifications to the reconnection rate. The close relation between variations in the inflow and the dynamics of the reconnection process we have identified in this simulation study could be further established through observations if we had simultaneous measurements in the reconnection outflow and inflow. This could be accomplished for example, by modifying the configuration of MMS to include an upstream monitor, or through conjunctions of multiple spacecraft observatories.

Data Availability Statement

Replication data for this study is available at (Spinnangr, 2021).

Acknowledgments
This study was supported by NOTUR/NORSTOR under project NN9496K. CN and PT received support from the Research Council of Norway under contract 300865.

References

Akhavan-Tafti, M., Palmroth, M., Slavin, J. A., Battarbee, M., Ganse, U., Grandin, M., et al. (2020). Comparative analysis of the Vlasiator simulations and MMS observations of multiple X-line reconnection and flux transfer events. *Journal of Geophysical Research: Space Physics*, *125*(7), e2019JA027410. https://doi.org/10.1029/2019JA027410

Akhavan-Tafti, M., Slavin, J. A., Eastwood, J. P., Cassak, P. A., & Gershman, D. J. (2019). MMS multi-point analysis of FTE evolution: Physical characteristics and dynamics. *Journal of Geophysical Research: Space Physics*, *124*(7), 5376–5395. https://doi.org/10.1029/2018JA026311

Burch, J. L., & Phan, T. D. (2016). Magnetic reconnection at the dayside magnetopause: Advances with MMS. *Geophysical Research Letters*, *43*(16), 8327–8338. https://doi.org/10.1002/2016GL069787

Burch, J. L., Torbert, R. B., Phan, T. D., Chen, L. J., Moore, T. E., Ergun, R. E., & Chandler, M. (2016). Electron-scale measurements of magnetic reconnection in space. *Science*, *352*(6290), aaf2939. https://doi.org/10.1126/science.aaf2939

Cassak, P. A., & Fuselier, S. A. (2016). *Reconnection at Earth's dayside magnetopause* (pp. 213–276). https://doi.org/10.1007/978-3-319-26432-5_6

Cassak, P. A., Liu, Y. H., & Shay, M. A. (2017). *A review of the 0.1 reconnection rate problem*. (Vol. 83). Cambridge University Press. https://doi.org/10.1017/S0022377817000666

Cassak, P. A., & Shay, M. A. (2007). Scaling of asymmetric magnetic reconnection: General theory and collisional simulations. *Physics of Plasmas*, *14*(10), 102114. https://doi.org/10.1063/1.2795630

Chen, L. J., Hesse, M., Wang, S., Gershman, D., Ergun, R. E., Burch, J., et al. (2017). Electron diffusion region during magnetopause reconnection with an intermediate guide field: Magnetospheric multiscale observations. *Journal of Geophysical Research: Space Physics*, *122*(5), 5235–5246. https://doi.org/10.1002/2017JA024004

Comisso, L. & Bhattacharjee, A. (2016). On the value of the reconnection rate. *Journal of Plasma Physics*, *82*(6), 1–9. https://doi.org/10.1017/S002237781600101X

Dargent, J., Aunai, N., Lavraud, B., Toledo-Redondo, S., & Califano, F. (2019). Signatures of cold ions in a kinetic simulation of the reconnecting magnetopause. *Journal of Geophysical Research: Space Physics*, *124*(4), 2497–2514. https://doi.org/10.1029/2018JA026343

Dargent, J., Aunai, N., Lavraud, B., Toledo-Redondo, S., & Califano, F. (2020). Simulation of plasmaspheric plume impact on dayside magnetic reconnection. *Geophysical Research Letters*, *47*(4), e2019GL086546. https://doi.org/10.1029/2019GL086546

Dargent, J., Aunai, N., Lavraud, B., Toledo-Redondo, S., Shay, M. A., Cassak, P. A., & Malakit, K. (2017). Kinetic simulation of asymmetric magnetic reconnection with cold ions. *Journal of Geophysical Research: Space Physics*, *122*(5), 5290–5306. https://doi.org/10.1002/2016JA023831

Drake, J. F., Shay, M. A., & Swisdak, M. (2008). The Hall fields and fast magnetic reconnection. *Physics of Plasmas*, *15*(4), 042306. https://doi.org/10.1063/1.2901194

Drake, J. F., Swisdak, M., Schoeffler, K. M., Rogers, B. N., & Kobayashi, S. (2006). Formation of secondary islands during magnetic reconnection. *Geophysical Research Letters*, *33*(13). https://doi.org/10.1029/2006GL025957

Fuselier, S. A., Trattner, K. J., & Petrinec, S. M. (2011). Antiparallel and component reconnection at the dayside magnetopause. *Journal of Geophysical Research*, *116*(A10). https://doi.org/10.1029/2011JA016888

Fuselier, S. A., Vines, S. K., Burch, J. L., Petrinec, S. M., Trattner, K. J., Cassak, P. A., et al. (2017). Large scale characteristics of reconnection diffusion regions and associated magnetopause crossings observed by MMS. *Journal of Geophysical Research: Space Physics*, *122*(5), 5466–5486. https://doi.org/10.1002/2017JA024024

Goldman, M. V., Lapenta, G., Newman, D. L., Markidis, S., & Che, H. (2011). Jet deflection by very weak guide fields during magnetic reconnection. *Physical Review Letters*, *107*(13), 135001. https://doi.org/10.1103/PhysRevLett.107.135001

Hesse, M., Liu, Y. H., Chen, L. J., Bessho, N., Kuznetsova, M., Birn, J., & Burch, J. L. (2016). On the electron diffusion region in asymmetric reconnection with a guide magnetic field. *Geophysical Research Letters*, *43*(6), 2359–2364. https://doi.org/10.1002/2016GL068373

Hesse, M., Norgren, C., Tenfjord, P., Burch, J. L., Liu, Y. H., Bessho, N., et al. (2021). A new look at the electron diffusion region in asymmetric magnetic reconnection. *Journal of Geophysical Research: Space Physics*, *126*(2), e2020JA028456. https://doi.org/10.1029/2020JA028456

Hesse, M., Schindler, K., Birn, J., & Kuznetsova, M. (1999). The diffusion region in collisionless magnetic reconnection. *Physics of Plasmas*, *6*(5), 1781–1795. https://doi.org/10.1063/1.873436

Hesse, M., Zenitani, S., & Klimas, A. (2008). The structure of the electron outflow jet in collisionless magnetic reconnection. *Physics of Plasmas*, *15*(11), 112102. https://doi.org/10.1063/1.3006341

Huba, J. D. (2005). Hall magnetic reconnection: Guide field dependence. *Physics of Plasmas*, *12*(1), 012322. https://doi.org/10.1063/1.1834592

Kolstø, H., Hesse, M., Norgren, C., Tenfjord, P., Spinnangr, S. F., & Kwagala, N. (2020a). Collisionless magnetic reconnection in an asymmetric oxygen density configuration. *Geophysical Research Letters*, *47*(1), e2019GL085359. https://doi.org/10.1029/2019GL085359

Kolstø, H., Hesse, M., Norgren, C., Tenfjord, P., Spinnangr, S. F., & Kwagala, N. (2020b). On the impact of a streaming oxygen population on collisionless magnetic reconnection. *Geophysical Research Letters*, *47*(22), e2020GL089462. https://doi.org/10.1029/2020GL089462

Liu, J., Angelopoulos, V., Runov, A., & Zhou, X. Z. (2013). On the current sheets surrounding dipolarizing flux bundles in the magnetotail: The case for wedgelets. *Journal of Geophysical Research: Space Physics*, *118*(5), 2000–2020. https://doi.org/10.1002/jgra.50092

Liu, Y. H., Hesse, M., Guo, F., Daughton, W., Li, H., Cassak, P. A., & Shay, M. A. (2017). Why does steady-state magnetic reconnection have a maximum local rate of order 0.1? *Physical Review Letters*, *118*(8), 085101. https://doi.org/10.1103/PhysRevLett.118.085101

Norgren, C., Tenfjord, P., Hesse, M., Toledo-Redondo, S., Li, W.-Y., Xu, Y., et al. (2021). On the presence and thermalization of cold ions in the exhaust of antiparallel symmetric reconnection. *Frontiers in Astronomy and Space Sciences*, *8*. https://doi.org/10.3389/fspas.2021.730061

Phan, T. D., Drake, J. F., Shay, M. A., Mozer, F. S., & Eastwood, J. P. (2007). Evidence for an elongated (>60 ion skin depths) electron diffusion region during fast magnetic reconnection. *Physical Review Letters*, *99*(25), 255002. https://doi.org/10.1103/PhysRevLett.99.255002

Poh, G., Slavin, J. A., Lu, S., Le, G., Ozturk, D. S., Sun, W. J., et al. (2019). Dissipation of earthward propagating flux rope through re-reconnection with geomagnetic field: An MMS case study. *Journal of Geophysical Research: Space Physics*, *124*(9), 7477–7493. https://doi.org/10.1029/2018JA026451

Pritchett, P. L. (2005). Onset and saturation of guide-field magnetic reconnection. *Physics of Plasmas*, *12*(6), 062301. https://doi.org/10.1063/1.1914309

Pritchett, P. L., & Coroniti, F. V. (2004). Three-dimensional collisionless magnetic reconnection in the presence of a guide field. *Journal of Geophysical Research*, *109*(A1). https://doi.org/10.1029/2003JA009999

Pritchett, P. L., & Mozer, F. S. (2009). Asymmetric magnetic reconnection in the presence of a guide field. *Journal of Geophysical Research*, *114*(11). https://doi.org/10.1029/2009JA014343

Ricci, P., Brackbill, J. U., Daughton, W., & Lapenta, G. (2004). Collisionless magnetic reconnection in the presence of a guide field. *Physics of Plasmas*, *11*(8), 4102–4114. https://doi.org/10.1063/1.1768552

Shuster, J. R., Chen, L. J., Hesse, M., Argall, M. R., Daughton, W., Torbert, R. B., & Bessho, N. (2015). Spatiotemporal evolution of electron characteristics in the electron diffusion region of magnetic reconnection: Implications for acceleration and heating. *Geophysical Research Letters*, *42*(8), 2586–2593. https://doi.org/10.1002/2015GL063601

Spinnangr, S. F. (2021). *Replication data for: Asymmetrically varying guide field during magnetic reconnection: Particle-In-Cell simulations*. DataverseNO. https://doi.org/10.18710/WGWLSE

Spinnangr, S. F., Hesse, M., Tenfjord, P., Norgren, C., Kolstø, H. M., Kwagala, N. K., & Jørgensen, T. M. (2021). The micro-macro coupling of mass-loading in symmetric magnetic reconnection with cold ions. *Geophysical Research Letters*, *48*(13). https://doi.org/10.1029/2020GL090690

Swisdak, M., Drake, J. F., Shay, M. A., & McIlhargey, J. G. (2005). Transition from antiparallel to component magnetic reconnection. *Journal of Geophysical Research*, *110*(A5). https://doi.org/10.1029/2004JA010748

Swisdak, M., Rogers, B. N., Drake, J. F., & Shay, M. A. (2003). Diamagnetic suppression of component magnetic reconnection at the magnetopause. *Journal of Geophysical Research*, *108*(A5). https://doi.org/10.1029/2002JA009726

Tenfjord, P., Hesse, M., & Norgren, C. (2018). The formation of an oxygen wave by magnetic reconnection. *Journal of Geophysical Research: Space Physics*, *123*(11), 9370–9380. https://doi.org/10.1029/2018JA026026

Tenfjord, P., Hesse, M., Norgren, C., Spinnangr, S. F., & Kolstø, H. (2019). The impact of oxygen on the reconnection rate. *Geophysical Research Letters*, *46*(12), 6195–6203. https://doi.org/10.1029/2019GL082175

Tenfjord, P., Hesse, M., Norgren, C., Spinnangr, S. F., Kolstø, H., & Kwagala, N. (2020). Interaction of cold streaming protons with the reconnection process. *Journal of Geophysical Research: Space Physics*, *125*(6), e2019JA027619. https://doi.org/10.1029/2019JA027619

Toledo-Redondo, S., André, M., Aunai, N., Chappell, C. R., Dargent, J., Fuselier, S. A., et al. (2021). Impacts of ionospheric ions on magnetic reconnection and Earth's magnetosphere dynamics. *Reviews of Geophysics*, *59*(3), e2020RG000707. https://doi.org/10.1029/2020rg000707

Torbert, R. B., Burch, J. L., Phan, T. D., Hesse, M., Argall, M. R., Shuster, J., et al. (2018). Electron-scale dynamics of the diffusion region during symmetric magnetic reconnection in space. *Science*, *362*(6421), 1391–1395. https://doi.org/10.1126/science.aat2998

Trattner, K. J., Burch, J. L., Ergun, R., Eriksson, S., Fuselier, S. A., Giles, B. L., et al. (2017). The MMS dayside magnetic reconnection locations during phase 1 and their relation to the predictions of the maximum magnetic shear model. *Journal of Geophysical Research: Space Physics*, *122*(12), 11991–12005. https://doi.org/10.1002/2017JA024488

Trattner, K. J., Mulcock, J. S., Petrinec, S. M., & Fuselier, S. A. (2007). Probing the boundary between antiparallel and component reconnection during southward interplanetary magnetic field conditions. *Journal of Geophysical Research*, *112*(8), A08210. https://doi.org/10.1029/2007JA012270

Wilder, F. D., Ergun, R. E., Burch, J. L., Ahmadi, N., Eriksson, S., Phan, T. D., et al. (2018). The role of the parallel electric field in electron-scale dissipation at reconnecting currents in the magnetosheath. *Journal of Geophysical Research: Space Physics*, *123*(8), 6533–6547. https://doi.org/10.1029/2018JA025529

Zhou, M., Berchem, J., Walker, R. J., El-Alaoui, M., Deng, X., Cazzola, E., et al. (2017). Coalescence of macroscopic flux ropes at the subsolar magnetopause: Magnetospheric multiscale observations. *Physical Review Letters*, *119*(5), 1–6. https://doi.org/10.1103/PhysRevLett.119.055101